Quartic anharmonicity and anomalous thermal conductivity in cubic antiperovskites A_3BO (A = K, Rb; B = Br, Au)

Yinchang Zhao,[1,*] Chao Lian,[2] Shuming Zeng,[3] Zhenhong Dai,[1,†] Sheng Meng,[4,‡] and Jun Ni[3,5,§]

[1]*Department of Physics, Yantai University, Yantai 264005, People's Republic of China*

[2]*Oden Institute and Department of Physics, University of Texas at Austin, Austin, Texas 78712, USA*

[3]*State Key Laboratory of Low-Dimensional Quantum Physics, Department of Physics, Tsinghua University, Beijing 100084, People's Republic of China*

[4]*Beijing National Laboratory for Condensed Matter Physics and Institute of Physics, Chinese Academy of Sciences, Beijing 100190, People's Republic of China*

[5]*Frontier Science Center for Quantum Information, Beijing 100084, People's Republic of China*

(Received 9 January 2020; revised manuscript received 22 March 2020; accepted 17 April 2020; published 7 May 2020)

We use *ab initio* self-consistent phonon theory combined with compressive sensing techniques to investigate the role of quartic anharmonicity in the lattice dynamics and thermal transport properties of the cubic antiperovskites A_3BO (A = K, Rb; B = Br, Au). Our findings indicate that the strong quartic anharmonicity of alkali-metal atoms plays a crucial role in the phonon quasiparticles free from imaginary frequencies in K_3BrO, Rb_3BrO, and Rb_3AuO, and gives rise to an evident hardening of vibrational frequencies of the low-lying modes in K_3AuO. Based on these results, the lattice thermal transport properties are predicted through the Boltzmann transport equation within the relaxation time approximation. The results exhibit that the four cubic antiperovskites have remarkably low thermal conductivities κ_L, e.g., 0.73–1.70 W/mK at 300 K, and an anomalously weak temperature dependence of the κ_L, e.g., $\kappa_L \sim T^{-0.3}$, of which the latter has not been reported in normal perovskites and other conventional semiconductors to date. We demonstrate that the strong three-phonon scattering along with strong quartic anharmonic renormalization of the soft modes and the presence of high-frequency dispersive optical modes are responsible for the thermal conductivity spectrum $\kappa_L(\omega)$ and thus the low κ_L and its anomalously weak temperature dependence.

DOI: 10.1103/PhysRevB.101.184303

I. INTRODUCTION

The lattice anharmonic effect plays a significant role in a series of physical phenomena including phonon frequency shift, temperature dependence of vibrational frequencies, thermal expansion, structural phase transformation, and ferroelectricity [1]. At the same time, it also gives rise to finite phonon lifetime and lattice thermal conductivity κ_L, which is a crucial quantity in optimization of the dimensionless figure of merit ZT for thermoelectric materials [2–5]. For different materials, due to different magnitudes of lattice anharmonicity the associated physical properties display huge dissimilarities. In general, thermoelectric and ferroelectric materials possess strong anharmonic effects, as verified by the inelastic-scattering spectra of neutrons and the ultralow values of κ_L [6–8], while covalent crystals such as diamond and graphene have fairly weak anharmonicity and consequently exhibit excellent thermal transport performances [9,10]. In addition, lattice anharmonicity can also lead to important effects in superconductors [11,12], materials under extreme conditions [13,14], etc.

Several methods for calculating anharmonic effects of solids at finite temperature have been developed in the past decade. In the temperature-dependent effective potential method [15,16], a model Hamiltonian is fitted based on the trajectory of the forces computed from *ab initio* molecular dynamics (AIMD), in which the harmonic or anharmonic terms can be included. The self-consistent *ab initio* lattice dynamics method [17] constructs a thermally averaged effective harmonic Hamiltonian to capture the anharmonic effects via an iterative procedure. The stochastic self-consistent harmonic approximation [18] is a method that minimizes the free energy of an ensemble of harmonic oscillators in the real potential with respect to the harmonic force constants and compound structure. Finally, the combination of the self-consistent phonon (SCP) theory [19] with the compressive sensing (CS) lattice dynamics [20–22] is a recently proposed approach to estimate the anharmonicity [23–25], in which the anharmonic frequency is calculated from the pole of the Green's function using the cubic and quartic interatomic force constants (IFCs) extracted by the CS techniques from first-principles calculations.

Recently, the roles of anharmonicity in the lattice dynamics and thermal transport properties of cubic perovskite

*y.zhao@ytu.edu.cn
†zhdai@ytu.edu.cn
‡smeng@iphy.ac.cn
§junni@mail.tsinghua.edu.cn

 ©2020 American Physical Society

$SrTiO_3$ [23,24], empty perovskite ScF_3 [26,27], and type-I clathrate $Ba_8Ga_{16}Ge_{30}$ [25] have been systemically investigated, which demonstrated that these materials are typical strong anharmonic crystals with anomalous lattice thermal conductivities κ_L. In this work, to further explore the anharmonic effects and related physical properties, we turn to the antiperovskites, which, also known as inverse perovskites, are a class of crystals that possess perovskite configurations but with anions replaced by cations and vice versa [28]. To date, the strong anharmonicity captured in perovskites has not been reported in any antiperovskite structures, although many interesting properties such as superionic conductivity [29–31], topological electronic states [32,33], zero or negative thermal expansion [34–36], piezomagnetic effects [37], and superconductivity [38] have been studied in this type of materials. Of various antiperovskites, the cubic structures with $Pm\bar{3}m$ symmetry, such as K_3BrO, K_3AuO, Rb_3BrO, Rr_3AuO, Mg_3AsN, Mg_3SbN, Ni_3MgC, and Sr_3SnO, have attracted great research interest due to their simple configurations [39–44]. In addition, the usual candidates for thermoelectric applications are the semiconductors with low thermal conductivity [2–5], and the thermal transport performance of a semiconductor is mainly determined by the lattice thermal conductivity κ_L. Therefore, the anharmonic effects and related thermal transport in the semiconducting cubic antiperovskites are focused first, although other Dirac antiperovskites such as Sr_3SnO and Sr_3PbO have also attracted great interest [45].

In this paper, we take the cubic antiperovskites A_3BO (A = K, Rb; B = Br, Au), which are semiconducting materials with a band gap between 0.24 and 0.89 eV [46], as examples to systematically investigate the role of the anharmonicity in the lattice dynamics and thermal transport properties based on the ab initio SCP theory combined with the CS techniques. Our key findings are that (i) the strong quartic anharmonicity of alkali-metal atoms plays a significant role in the phonons free from imaginary frequencies in K_3BrO, Rb_3BrO, and Rb_3AuO, and gives rise to an evident hardening of the low-lying modes in K_3AuO, and (ii) remarkably low thermal conductivities κ_L with an anomalously weak temperature dependence of $\kappa_L \sim T^{-0.3}$ are obtained in these antiperovskite structures.

II. METHODOLOGY

All calculations are carried out using density functional theory (DFT) implemented in VASP [47,48], with the projector augmented wave (PAW) potentials [49], the Perdew-Burke-Ernzerhof functional revised for solids (PBEsol) [50], and a cutoff energy of 550 eV. The unit cell is fully optimized until the force on each atom is less than 10^{-6} eV/Å, with a **k**-point of $12 \times 12 \times 12$ and a total energy convergence of 10^{-8} eV. The dielectric tensors and Born effective charges required for the nonanalytic part of the dynamical matrix are calculated from density functional perturbation theory [51]. The harmonic IFCs are generated within a $2 \times 2 \times 2$ supercell by the finite-displacement approach [52] with a displacement of 0.01 Å, as coded in the ALAMODE package [23,53]. The cubic and quartic IFCs are produced through the CS lattice dynamics method, in which the crucial anharmonic terms are computed from the sparse solution extracted from the incomplete data [54]. In detail, we first sample 80 snapshots from a 4000-step AIMD simulated at 300 K with 2-fs time step in a $2 \times 2 \times 2$ supercell, and displace the atoms in each sampled snapshot by 0.12 Å along random directions to gain the quasirandom configurations. Then, we compute the Hellmann-Feynman forces of each quasirandom configuration within a $6 \times 6 \times 6$ **k**-point using the static DFT. Finally, based on the data set comprising of displacements and forces of the 80 quasirandom configurations, the anharmonic IFCs are estimated through the least absolute shrinkage and selection operator (LASSO) technique [23,25]. Here, the anharmonic IFCs up to sixth order, all terms for harmonic and cubic IFCs, and the terms inside the fifth-nearest-neighbor (fourth-nearest neighbor) shell for quartic (quintic and sextic) IFCs are considered, and the trivial four-body terms for quartic IFCs and the multibody (>2 body) terms for quintic and sextic IFCs are excluded. As a result, there are 698, 2445, 43, and 125 irreducible terms for the cubic, quartic, quintic, and sextic IFCs, respectively, given the constraints of symmetry operations and translational invariance.

From the gained harmonic, cubic, and quartic IFCs, the SCP calculations are performed to obtain the anharmonic frequencies. Due to the usage of $2 \times 2 \times 2$ supercells in generating IFCs, the reciprocal-to-real-space Fourier interpolation is limited to a $2 \times 2 \times 2$ **q**-point. Consequently, the $\mathbf{q_1}$-mesh, which is used for the inner loop of the SCP equation, as listed in Eqs. (20)– (23) in Ref. [23], is changed to achieve the convergence of anharmonic frequencies. The off-diagonal elements of phonon self-energy are included in the SCP calculations, and the mixing parameter $\alpha = 0.1$ (0.05) is used in the SCP iteration for temperature above (below) 300 K. Finally, the lattice thermal conductivity is estimated within a $12 \times 12 \times 12$ **q**-mesh by the Boltzmann transport equation (BTE) based on the relaxation time approximation (RTA), where the three-phonon scattering is calculated from the imaginary part of phonon self-energy resulting from the cubic IFCs, and the anharmonic frequencies and eigenvectors are taken as inputs.

III. RESULTS AND DISCUSSION

The PBEsol optimized lattice constants for K_3BrO, K_3AuO, Rb_3BrO, and Rr_3AuO are 5.175, 5.206, 5.451, and 5.477 Å, respectively, which are in accordance with the experimental values of 5.213, 5.240, 5.465, and 5.501 Å, respectively [39–41]. The calculated dielectric tensors and Born effective charges of the four cubic antiperovskites are listed in Table I. As an example, the dielectric tensor and Born effective charges of K_3BrO have the values of $\epsilon^{\infty} = 3.056$, $Z^*(\mathrm{K})_{\parallel} = 1.221$, $Z^*(\mathrm{K})_{\perp} = 1.111$, $Z^*(\mathrm{Br}) = -1.208$, and $Z^*(\mathrm{O}) = -2.236$.

For vibrational properties, we start from the harmonic phonon dispersion relations of the four cubic antiperovskites, as plotted by the cyan lines in Fig. 1. Evidently, the low-lying modes around the M $(\frac{1}{2}, \frac{1}{2}, 0)$ and R $(\frac{1}{2}, \frac{1}{2}, \frac{1}{2})$ points in K_3BrO, Rb_3BrO, and Rr_3AuO are unstable ($\omega_{\mathbf{q}}^2 < 0$), e.g., with the respective imaginary frequencies of $27.8i$ ($28.1i$) cm^{-1}, $27.3i$ ($27.4i$) cm^{-1}, and $21.8i$ ($22.3i$) cm^{-1} for the softest mode A_{2g} (T_{1g}) at the M (R) point. Based on the harmonic dispersion results, only K_3AuO is dynamically stable, and its

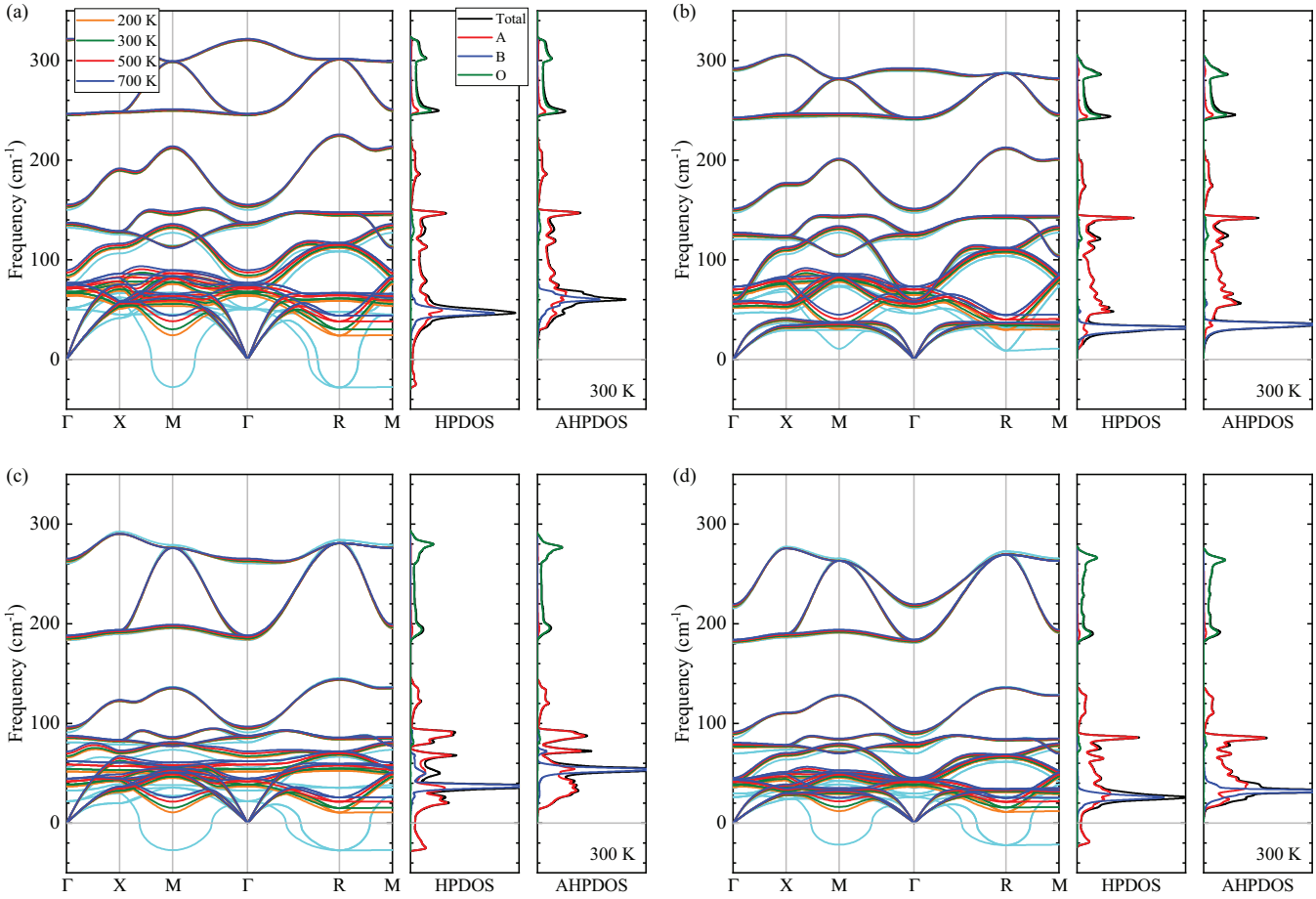

FIG. 1. Harmonic and anharmonic phonon dispersions, harmonic phonon density of states (HPDOS), and anharmonic phonon density of states (AHPDOS) for (a) K_3BrO, (b) K_3AuO, (c) Rb_3BrO, and (d) Rr_3AuO. In phonon dispersions, the orange, olive, red, and blue lines represent the anharmonic dispersion relations calculated using the SCP theory within an $8 \times 8 \times 8$ $\mathbf{q_1}$-point at 200, 300, 500, and 700 K, respectively, while the harmonic dispersion is plotted by the cyan line. In both HPDOS and AHPDOS, the red, blue, and olive lines represent the partial phonon density of states of the alkali-metal atoms, bromine or gold atoms, and oxygen atoms, respectively. For the AHPDOS, only the result at 300 K is displayed.

corresponding low-lying modes have the frequencies 10.6 and 8.7 cm^{-1} at the M and R points, respectively, as shown in Fig. 1(b). In addition, the calculated harmonic phonon density of states (HPDOS) reveals that the imaginary phonons in K_3BrO, Rb_3BrO, and Rr_3AuO are contributed completely by the collective motions of the alkali-metal atoms. For instance, the atomic vibrations of the low-lying mode A_{2g} (T_{1g}) at the M (R) point are related to the motions of only the alkali-metal atoms, as shown in Figs. 2(a) and 2(b).

TABLE I. Calculated lattice constants (a^{opt}), dielectric tensors (ϵ^{∞}), and Born effective charges (Z^*) for antiperovskites K_3BrO, K_3AuO, Rb_3BrO, and Rr_3AuO. The experimental lattice constants a^{expt} adapted from Refs. [39–41] are also listed for comparison.

A_3BO	K_3BrO	K_3AuO	Rb_3BrO	Rb_3AuO
a^{opt} (Å)	5.175	5.206	5.451	5.477
a^{expt} (Å)	5.213	5.240	5.465	5.501
ϵ^{∞}	3.056	5.265	3.497	9.522
$Z^*(A)_{\parallel}$	1.221	0.901	1.405	0.964
$Z^*(A)_{\perp}$	1.111	1.289	1.129	1.384
$Z^*(B)$	−1.208	−0.964	−1.246	−1.008
$Z^*(O)$	−2.236	−2.515	−2.417	−2.723

The anharmonic phonon dispersion relations at various temperatures calculated using the SCP theory within an $8 \times 8 \times 8$ $\mathbf{q_1}$-point grid are plotted in Fig. 1. To check the convergence of the obtained anharmonic phonon dispersions, the anharmonic frequencies at 300 K are calculated within different $\mathbf{q_1}$-point grids. The frequencies of the softest optical mode T_{2u} at the Γ (0,0,0) point, the low-lying mode A_{2g} at the M point, and the low-lying mode T_{1g} at the R point in four cubic antiperovskites K_3BrO, K_3AuO, Rb_3BrO, and Rr_3AuO are listed in Table II. These results indicate that a $4 \times 4 \times 4$ $\mathbf{q_1}$-point grid is dense enough to obtain the convergent anharmonic frequencies, while a less dense $2 \times 2 \times 2$ $\mathbf{q_1}$-point overestimates the frequency values. Therefore, the anharmonic phonon dispersions calculated within the $8 \times 8 \times 8$ $\mathbf{q_1}$-point in Fig. 1 are well convergent. Obviously, due to the large frequency shifts of the low-lying modes, there is no imaginary frequency observed in K_3BrO, Rb_3BrO, and

TABLE II. Anharmonic phonon frequencies (cm^{-1}) of the softest optical mode T_{2u} at the Γ point, the low-lying mode A_{2g} at the M point, and the low-lying mode T_{1g} at the R point in four cubic antiperovskites K_3BrO, K_3AuO, Rb_3BrO, and Rr_3AuO calculated using the SCP equation at 300 K within different $\mathbf{q_1}$-point grids. The harmonic phonon frequencies are also listed for comparison.

toprule	K_3BrO			K_3AuO			Rb_3BrO			Rr_3AuO		
$\mathbf{q_1}$-point grids	T_{2u}	A_{2g}	T_{1g}	T_{2u}	A_{2g}	T_{1g}	T_{2u}	A_{2g}	T_{1g}	T_{2u}	A_{2g}	T_{1g}
$2 \times 2 \times 2$	66.8	31.7	31.5	53.4	35.7	34.7	39.1	17.1	17.0	38.7	17.8	17.3
$4 \times 4 \times 4$	66.4	30.0	29.8	53.2	35.6	33.8	38.5	15.1	14.9	38.1	16.1	15.5
$6 \times 6 \times 6$	66.5	30.1	29.9	53.2	35.6	33.8	38.6	15.1	14.9	38.1	16.0	15.5
$8 \times 8 \times 8$	66.5	30.2	30.0	53.2	35.6	33.8	38.6	15.2	15.0	38.1	16.0	15.5
$10 \times 10 \times 10$	66.5	30.2	30.0	53.2	35.6	33.8	38.6	15.2	15.0	38.1	16.0	15.5
Harmonic phonon	50.1	27.8i	28.1i	46.1	10.6	8.7	21.8	27.3i	27.4i	25.9	21.8i	22.3i

Rr_3AuO based on the SCP results. Meanwhile, the low-lying modes in K_3AuO are also significantly hardened, as shown in Fig. 1.

In the present SCP theory, since the frequency shifts induced by the cubic term and the quasiharmonic effect are neglected, only the quartic anharmonic effect, which generally boosts the frequencies of the low-lying modes because of the positive and dominant contribution from the diagonal term of the quartic coefficient, is taken into consideration in the SCP calculations for capturing the lattice anharmonicity [23–25]. In combination with the imaginary phonon

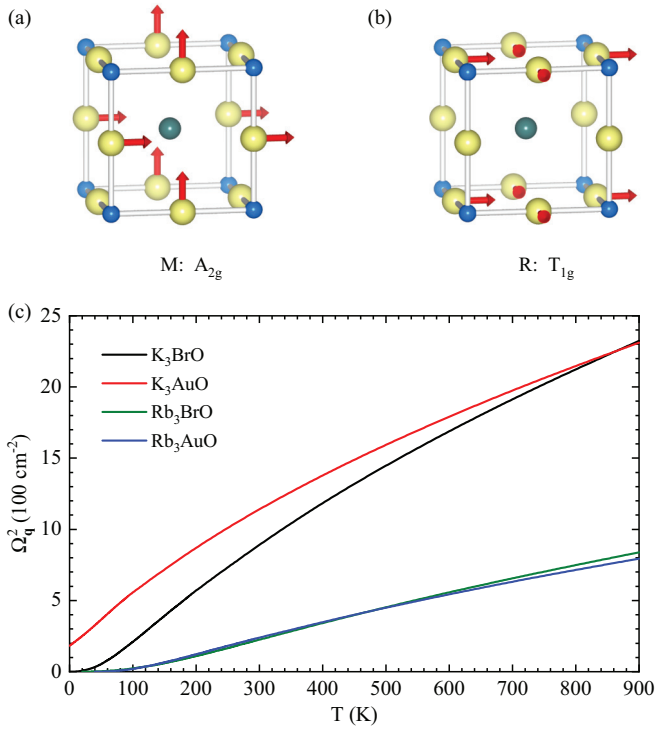

FIG. 2. Atomic vibrations of (a) the A_{2g} mode at the M point and (b) the T_{1g} mode at the R point in each cubic antiperovskite. The big yellow, medium dark cyan, and small blue spheres represent the alkali-metal, bromine or gold, and oxygen atoms, respectively. The red arrows denote the atomic motions. (c) Temperature dependence of the squared frequencies of the T_{1g} mode in four antiperovskites obtained from the SCP calculations within a $10 \times 10 \times 10$ $\mathbf{q_1}$-point.

frequencies arising completely from alkali-metal atoms in the harmonic phonon calculations, the imaginary-frequency-absent anharmonic phonon dispersions calculated by the present SCP theory indicate that the alkali-metal atoms in the four cubic antiperovskites have significantly strong quartic anharmonicity, which plays a crucial role in the structural stabilities of K_3BrO, Rb_3BrO, and Rr_3AuO. In addition, the calculated anharmonic phonon density of states (AHPDOS) at 300 K shows that the collective motions of alkali-metal atoms and bromine and gold atoms dominate the acoustic modes and low-frequency optical modes, while the three high-frequency phonon branches are governed primarily by the motions of oxygen atoms, as shown in Fig. 1.

Furthermore, one can observe that the low-frequency anharmonic modes, e.g., $\Omega_{\mathbf{q}} < 180$ cm^{-1} for K_3BrO and K_3AuO and $\Omega_{\mathbf{q}} < 100$ cm^{-1} for Rb_3BrO and Rb_3AuO, harden with the increase of temperature, while the high-frequency modes have relatively small anharmonic renormalization, as shown in Fig. 1. To reveal the temperature dependence of the low-frequency anharmonic phonons quantitatively, we focus on the low-lying T_{1g} mode at the R point, which is the softest mode in the region away from the Brillouin zone center, as shown in Fig. 1 and Table II. The squared phonon frequencies $\Omega_{\mathbf{q}}^2$ of the T_{1g} mode as functions of temperature in the four cubic antiperovskites are plotted in Fig. 2(c), which are obtained using a $10 \times 10 \times 10$ $\mathbf{q_1}$-point grid. We find that these squared frequencies $\Omega_{\mathbf{q}}^2$ increase with the increasing temperature in each cubic antiperovskite. In particular, the $\Omega_{\mathbf{q}}^2$ values are close to zero at about 40 K in K_3BrO and 100 K in Rb_3BrO and Rb_3AuO, while the soft-mode frequency cannot reach zero in the present calculations within a finite $\mathbf{q_1}$-point [23,55]. In the cubic perovskite $SrTiO_3$, the similar soft mode at the R point is an antiferrodistortive (AFD) mode that drives the cubic-to-tetragonal phase transition at 105 K due to its freezing out [56–58]. The SCP calculation gives this cubic-to-tetragonal phase transition at 220 K according to the temperature at which the $\Omega_{\mathbf{q}}^2$ of the AFD mode reaches zero [23]. Similarly, the $\Omega_{\mathbf{q}}^2$ values close to zero in K_3BrO, Rb_3BrO, and Rb_3AuO demonstrate the freezing out of the T_{1g} mode, which implies a potential phase transition at very low temperature in these cubic antiperovskites, although there is no experimental result reported to date.

We now turn to the lattice thermal conductivity κ_L, which is estimated by the BTE within RTA through the

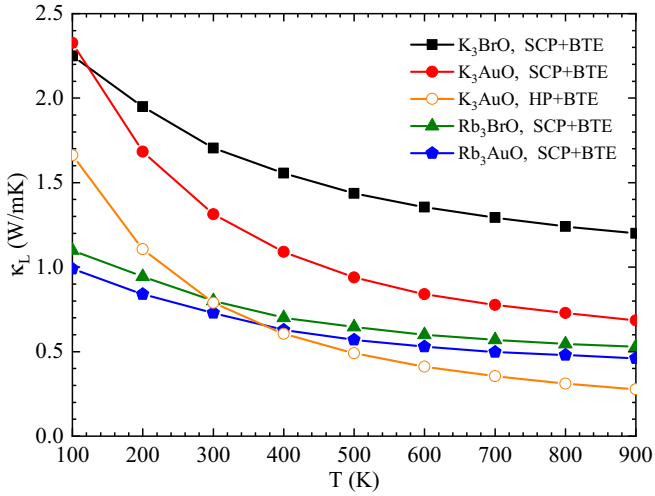

FIG. 3. Lattice thermal conductivity κ_L of the four cubic antiperovskites calculated by the SCP+BTE method. For K_3AuO, the HP+BTE result is also shown for comparison.

formula $\kappa_L^{\alpha\beta}(T) = (1/NV)\sum_q C_q(T)v_q^\alpha(T)v_q^\beta(T)\tau_q(T)$, where V, $C_q(T)$, $v_q(T)$, and $\tau_q(T)$ are the unit cell volume, mode specific heat, phonon group velocity, and phonon lifetime, respectively. The SCP frequencies and eigenvectors are employed as inputs for the BTE, and consequently $v_q(T) = \partial\Omega_q(T)/\partial\mathbf{q}$ also has temperature dependence. The phonon lifetime $\tau_q(T)$ is calculated by Matthiessen's rule $1/\tau_q = 1/\tau_q^{\text{anh}} + 1/\tau_q^{iso}$, where the anharmonic scattering rate $1/\tau_q^{\text{anh}}$ is obtained via the relation $1/\tau_q^{\text{anh}} = 2\Gamma_q(\Omega_q)$ from the phonon linewidth $\Gamma_q(\omega_q)$ computed by the imaginary part of the phonon self-energy from the cubic anharmonicity (see Eq. (18) in Ref. [23]), and the phonon-isotope scattering $1/\tau_q^{iso}$ is estimated in a manner of perturbation [59]. This SCP+BTE method is different from the conventional harmonic phonon-based BTE (HP+BTE) method, where the $v_q(T)$ and $\tau_q(T)$ are calculated using harmonic frequencies and eigenvectors as the ground state.

The calculated lattice thermal conductivities κ_L of the four cubic antiperovskites are plotted in Fig. 3, in which the values below 100 K are excluded since a latent phase transition will occur around 100 K in Rb_3BrO and Rb_3AuO based on above SCP calculations. For K_3AuO, the dual results of the HP+BTE and SCP+BTE methods are displayed, while only the SCP+BTE results are shown for K_3BrO, Rb_3BrO, and Rr_3AuO because the HP+BTE method is expired due to the presence of imaginary frequencies in their harmonic phonon dispersions. From the dual results in K_3AuO, one can find that the κ_L calculated by the SCP+BTE method is evidently higher than the value obtained by the HP+BTE method, which reveals the crucial effect of frequency renormalization on the thermal transport performance. Strikingly, the values of the κ_L for the four cubic antiperovskites are fairly low. For instance, the κ_L of K_3BrO, K_3AuO, Rb_3BrO, and Rr_3AuO obtained from the SCP+BTE calculations at 300 K are about 1.7, 1.31, 0.8, and 0.73 W/mK, respectively, which are much lower than the values of $\kappa_L \sim 9$–11 W/mK in the cubic perovskite $SrTiO_3$ [23,60,61] and $\kappa_L \sim 2$ W/mK in the typical thermoelectric material PbTe [62,63], and comparable to the results of $\kappa_L \sim 0.5$–1.5 W/mK in the full Heusler semiconductors [64] and $\kappa_L \sim 0.97$–1.31 W/mK in the type-I clathrate $Ba_8Ga_{16}Ge_{30}$ [25,65,66].

Another important point is that the κ_L calculated by the SCP+BTE method exhibits an anomalously weak temperature dependence in each cubic antiperovskite, especially in K_3BrO, Rb_3BrO, and Rr_3AuO. We can approximately describe the temperature dependence by a power law $\kappa_L \propto T^{-\alpha}$ with $\alpha \sim 0.3$ for K_3BrO, Rb_3BrO, and Rr_3AuO and $\alpha \sim 0.6$ for K_3AuO. Compared with previous results, the temperature dependence of the κ_L in K_3AuO is similar to that in cubic perovskite $SrTiO_3$ and empty perovskite ScF_3, where the κ_L follows a power law $\kappa_L \propto T^{-\alpha}$ with $\alpha \sim 0.6$–0.7 [26,60,61]. However, the power law close to $\kappa_L \propto T^{-0.3}$ in K_3BrO, Rb_3BrO, and Rr_3AuO has not been reported in any normal perovskites and other conventional semiconductors to date, which demonstrates an even weaker temperature dependence in the antiperovskites.

To elucidate the origins of the low κ_L, the anomalous temperature dependence of the κ_L, and the effect of the hardening of the soft modes on the κ_L, we analyze the thermal conductivity spectra $\kappa_L(\omega)$ and their cumulative values in the four cubic antiperovskites from different perspectives. K_3BrO is taken as an example to reveal the mechanism beyond the anomalous temperature dependence of the κ_L, and its SCP+BTE results of the thermal conductivity spectra $\kappa_L(\omega)$ with corresponding cumulative κ_L at 100 and 300 K are plotted in Fig. 4(a). It can be seen that the cumulative values at 100 and 300 K are almost equal at the frequency of 85 cm^{-1} due to the temperature-induced opposite changes in the $\kappa_L(\omega)$ between the two frequency ranges 0–36 and 66–85 cm^{-1}, and consequently the difference between the κ_L values at the two considered temperatures results primarily from the temperature-induced changes in the $\kappa_L(\omega)$ for the modes with frequencies above 85 cm^{-1}, as shown in Fig. 4(a). Generally, in the HP+BTE calculations [67], because of the changes in the Bose distribution function, the increase of temperature results in the enhanced three-phonon scattering, reduced phonon lifetime [68], and thus the declined thermal conductivity spectrum $\kappa_L(\omega)$. However, in the present SCP+BTE calculations, since the effect of the changes in the Bose distribution function is offset by the frequency enhancement caused by the strong quartic anharmonic renormalization (see Eq. (18) in Ref. [23]), the three-phonon scattering and phonon lifetimes of the soft modes (below 85 cm^{-1} in K_3BrO) are less sensitive to the increase of temperature (see Fig. S1 in the Supplemental Material [69]), which interprets the almost temperature-insensitive cumulative κ_L at 85 cm^{-1} shown in Fig. 4(a). Therefore, considering that the three-phonon scattering of the soft modes plays a significant role in the final κ_L, the temperature dependence of the κ_L obtained from the SCP+BTE calculations will be much deviated from the power law $\kappa_L \propto T^{-1}$ given by the conventional HP+BTE method, supporting the anomalously weak temperature dependence of $\kappa_L \propto T^{-0.3}$ in K_3BrO. In addition, it is worth noting that other effects such as thermal expansion and additional four-phonon scattering induced by the quartic anharmonicity also play important roles in determining the temperature dependence of the κ_L [70]. If these factors are included in estimating the lattice thermal transport, the temperature dependence of the

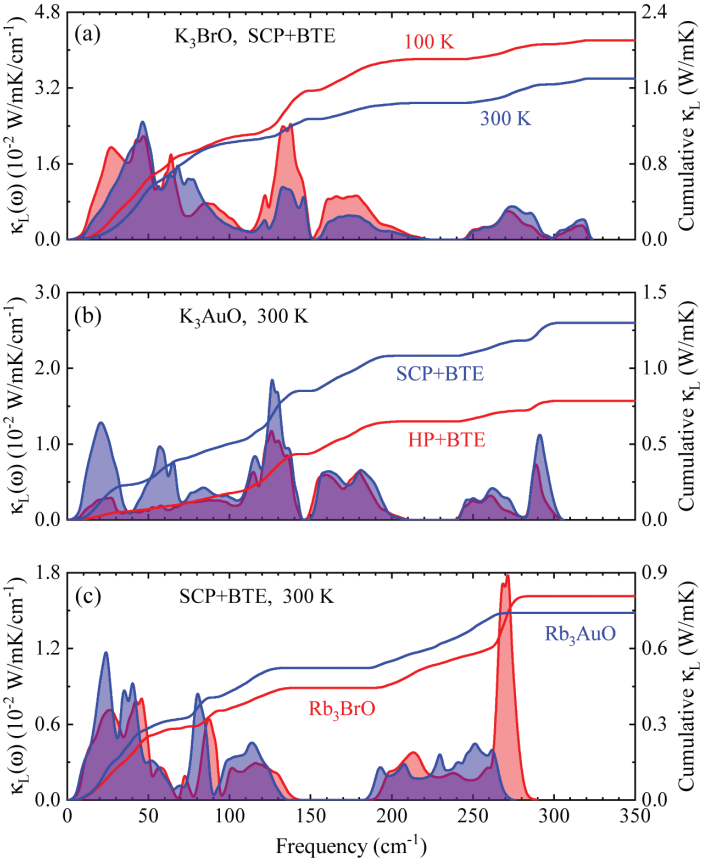

FIG. 4. Thermal conductivity spectra $\kappa_L(\omega)$ (the curves below which the areas are filled) and corresponding cumulative values (the bare curves). (a) The SCP+BTE results for K_3BrO at 100 and 300 K. (b) Comparison of the HP+BTE and SCP+BTE results for K_3AuO at 300 K. (c) The SCP+BTE results for Rb_3BrO and Rb_3AuO at 300 K.

κ_L may be somewhat different from the relationship of $\kappa_L \propto T^{-0.3}$, which indicates a potential limitation of the method used in the present calculations.

The dual κ_L values obtained from the HP+BTE and SCP+BTE calculations for K_3AuO preliminarily exhibit the effect of frequency renormalization on thermal transport, as shown in Fig. 3. To reveal the effect of the hardening of the soft modes on the κ_L in detail, we plot the HP+BTE and SCP+BTE calculated thermal conductivity spectra $\kappa_L(\omega)$ and cumulative κ_L at 300 K for K_3AuO in Fig. 4(b). Obviously, the difference between the two κ_L values computed by the two different methods arises mainly from the increase of the SCP+BTE calculated $\kappa_L(\omega)$ for the modes with frequencies below 145 cm^{-1}, relative to the $\kappa_L(\omega)$ obtained from the HP+BTE calculations, as shown in Fig. 4(b). Our analyses show that the anharmonic-renormalization-driven hardening of the soft modes gives rise to the reduction of three-phonon scattering and thus the enhancement of phonon lifetimes (see Fig. S2 in the Supplemental Material [69]), accounting for the method-induced changes in the $\kappa_L(\omega)$ for low-frequency modes. Finally, the SCP+BTE results of the spectra $\kappa_L(\omega)$ with cumulative values at 300 K for Rb_3BrO and Rb_3AuO are shown in Fig. 4(c). In contrast to that of Rb_3AuO, the $\kappa_L(\omega)$ of Rb_3BrO has a peak around the high frequency of 270 cm^{-1}, which causes the crossing of the two cumulative κ_L. The higher phonon lifetimes combined with higher group velocities of the modes with frequencies of about 270 cm^{-1} in Rb_3BrO explain the $\kappa_L(\omega)$ peak around 270 cm^{-1} in this material (see Fig. S3 in the Supplemental Material [69]).

Compared with the phonon lifetimes and group velocities in the typical thermoelectric material PbTe (see Figs. 3 and 4 in Ref. [62]), the phonon lifetimes of the soft modes in the four cubic antiperovskites are about half of those in PbTe, and the group velocities of the soft modes in K_3BrO are comparable to the values in PbTe while the values in K_3AuO, Rb_3BrO, and Rr_3AuO are about 30% lower than those in PbTe (see Figs. S1– S3 in the Supplemental Material [69]). These results mean that the κ_L in the four cubic antiperovskites should be about 25–50 % of the $\kappa_L \sim 2$ W/mK in PbTe. However, due to the existence of good dispersion, the high-frequency optical modes also play a role in the thermal transport properties in the four cubic antiperovskites, especially in Rb_3BrO, as shown in Fig. 4. Therefore, the $\kappa_L \sim 0.73$–1.70 W/mK at 300 K are finally obtained in these cubic antiperovskites.

IV. CONCLUSION

In conclusion, we have systematically investigated the role of quartic anharmonicity in the lattice dynamics and thermal transport properties of the cubic antiperovskites K_3BrO, K_3AuO, Rb_3BrO, and Rb_3AuO by using the *ab initio* SCP theory combined with the CS techniques. We discovered that the alkali-metal atoms in the four cubic antiperovskites have a strong quartic anharmonic effect, which plays a crucial role in the phonon dispersions free from imaginary frequencies in K_3BrO, Rb_3BrO, and Rb_3AuO, and leads to an evident hardening of the low-lying modes in K_3AuO. By analyzing the freezing out of the low-lying T_{1g} mode, a potential phase transition occurring at about 40 K in K_3BrO and 100 K in Rb_3BrO and Rb_3AuO is predicted based on the present SCP calculations, although there is no experimental result reported to date. Then the thermal conductivities κ_L are calculated through the SCP+BTE method, where the SCP frequencies and eigenvectors are taken as the inputs for the BTE. The calculations show that the κ_L in the four cubic antiperovskites are remarkably low, e.g., 0.73–1.70 W/mK at 300 K, and possess a power law close to $\kappa_L \propto T^{-0.3}$ for K_3BrO, Rb_3BrO, and Rr_3AuO. The relationship of $\kappa_L \propto T^{-0.3}$, which demonstrates an even weaker temperature dependence in the antiperovskites, has not been reported in any normal perovskites and other conventional semiconductors where the usually reported power laws are $\kappa_L \propto T^{-0.6}$ and $\kappa_L \propto T^{-1}$, respectively. Our analyses reveal that the strong three-phonon scattering, low phonon velocity, and presence of high-frequency dispersive optical modes explain the thermal conductivity spectrum $\kappa_L(\omega)$ and thus the low κ_L, and the strong quartic anharmonic renormalization makes the three-phonon scattering of the soft modes almost insensitive to the increase of temperature, which dominates the anomalously weak temperature dependence of the κ_L.

ACKNOWLEDGMENTS

This research was supported by the National Natural Science Foundation of China under Grants No. 11704322, No. 11974302, No. 11774396, and No. 11774195; and the National Key Research and Development Program of China under Grants No. 2016YFA0300902 and No. 2016YFB0700102.

[1] D. C. Wallace, *Thermodynamics of Crystals* (Dover, Mineola, NY, 1972).
[2] G. J. Snyder and E. S. Toberer, in *Materials for Sustainable Energy*, edited by V. Dusastre (Nature Publishing Group, UK, 2010), pp. 101–110.
[3] Y. Zhao, Z. Dai, C. Lian, S. Zeng, G. Li, J. Ni, and S. Meng, Phys. Rev. Materials **1**, 065401 (2017).
[4] Y. Zhao, Z. Dai, C. Zhang, C. Lian, S. Zeng, G. Li, S. Meng, and J. Ni, Phys. Rev. B **95**, 014307 (2017).
[5] Y. Zhao, Z. Dai, C. Lian, and S. Meng, RSC Adv. **7**, 25803 (2017).
[6] T. Takabatake, K. Suekuni, T. Nakayama, and E. Kaneshita, Rev. Mod. Phys. **86**, 841(E) (2014).
[7] O. Delaire, J. Ma, K. Marty, A. F. May, M. A. McGuire, M. H. Du, D. J. Singh, A. Podlesnyak, G. Ehlers, M. D. Lumsden, and B. C. Sales, Nat. Mater. **10**, 614 (2011).
[8] L.-D. Zhao, S.-H. Lo, Y. Zhang, H. Sun, G. Tan, C. Uher, C. Wolverton, V. P. Dravid, and M. G. Kanatzidis, Nature (London) **508**, 373 (2014).
[9] A. Ward, D. A. Broido, D. A. Stewart, and G. Deinzer, Phys. Rev. B **80**, 125203 (2009).
[10] L. Lindsay, D. A. Broido, and N. Mingo, Phys. Rev. B **82**, 115427 (2010).
[11] R. Mankowsky, A. Subedi, M. Först, S. O. Mariager, M. Chollet, H. T. Lemke, J. S. Robinson, J. M. Glownia, M. P. Minitti, A. Frano, M. Fechner, N. A. Spaldin, T. Loew, B. Keimer, A. Georges, and A. Cavalleri, Nature (London) **516**, 71 (2014).
[12] Z. Hiroi, J.-i. Yamaura, and K. Hattori, J. Phys. Soc. Jpn. **81**, 011012 (2012).
[13] T. Sun, D.-B. Zhang, and R. M. Wentzcovitch, Phys. Rev. B **89**, 094109 (2014).
[14] W. Luo, B. Johansson, O. Eriksson, S. Arapan, P. Souvatzis, M. I. Katsnelson, and R. Ahuja, Proc. Natl. Acad. Sci. USA **107**, 9962 (2010).
[15] O. Hellman, I. A. Abrikosov, and S. I. Simak, Phys. Rev. B **84**, 180301(R) (2011).
[16] O. Hellman and I. A. Abrikosov, Phys. Rev. B **88**, 144301 (2013).
[17] P. Souvatzis, O. Eriksson, M. I. Katsnelson, and S. P. Rudin, Phys. Rev. Lett. **100**, 095901 (2008).
[18] I. Errea, M. Calandra, and F. Mauri, Phys. Rev. Lett. **111**, 177002 (2013).
[19] N. R. Werthamer, Phys. Rev. B **1**, 572 (1970).
[20] F. Zhou, W. Nielson, Y. Xia, and V. Ozoliņš, Phys. Rev. Lett. **113**, 185501 (2014).
[21] F. Zhou, W. Nielson, Y. Xia, and V. Ozoliņš, Phys. Rev. B **100**, 184308 (2019).
[22] F. Zhou, B. Sadigh, D. Åberg, Y. Xia, and V. Ozoliņš, Phys. Rev. B **100**, 184309 (2019).
[23] T. Tadano and S. Tsuneyuki, Phys. Rev. B **92**, 054301 (2015).
[24] T. Tadano and S. Tsuneyuki, J. Phys. Soc. Jpn. **87**, 041015 (2018).
[25] T. Tadano and S. Tsuneyuki, Phys. Rev. Lett. **120**, 105901 (2018).
[26] A. van Roekeghem, J. Carrete, and N. Mingo, Phys. Rev. B **94**, 020303(R) (2016).
[27] Y. Oba, T. Tadano, R. Akashi, and S. Tsuneyuki, Phys. Rev. Materials **3**, 033601 (2019).
[28] S. V. Krivovichev, Z. Kristallogr. Cryst. Mater. **223**, 109 (2008).
[29] Y. Zhao and L. L. Daemen, J. Am. Chem. Soc. **134**, 15042 (2012).
[30] Y. Zhang, Y. Zhao, and C. Chen, Phys. Rev. B **87**, 134303 (2013).
[31] Y. Li, W. Zhou, S. Xin, S. Li, J. Zhu, X. LÃ¼, Z. Cui, Q. Jia, J. Zhou, Y. Zhao, and J. B. Goodenough, Angew. Chem. Int. Ed. **55**, 9965 (2016).
[32] T. H. Hsieh, J. Liu, and L. Fu, Phys. Rev. B **90**, 081112(R) (2014).
[33] R. Yu, H. Weng, Z. Fang, X. Dai, and X. Hu, Phys. Rev. Lett. **115**, 036807 (2015).
[34] X. Song, Z. Sun, Q. Huang, M. Rettenmayr, X. Liu, M. Seyring, G. Li, G. Rao, and F. Yin, Adv. Mater. **23**, 4690 (2011).
[35] K. Takenaka and H. Takagi, Appl. Phys. Lett. **94**, 131904 (2009).
[36] K. Takenaka, K. Asano, M. Misawa, and H. Takagi, Appl. Phys. Lett. **92**, 011927 (2008).
[37] P. Lukashev, R. F. Sabirianov, and K. Belashchenko, Phys. Rev. B **78**, 184414 (2008).
[38] M. Oudah, A. Ikeda, J. N. Hausmann, S. Yonezawa, T. Fukumoto, S. Kobayashi, M. Sato, and Y. Maeno, Nat. Commun. **7**, 13617 (2016).
[39] M. Jansen, Chem. Soc. Rev. **37**, 1826 (2008).
[40] C. Feldmann and M. Jansen, Z. Anorg. Allg. Chem. **621**, 201 (1995).
[41] C. Feldmann and M. Jansen, Z. Anorg. Allg. Chem. **621**, 1907 (1995).
[42] R. H. Mitchell, *Perovskites: Modern and Ancient* (Almaz Press, Thunder Bay, Ontario, Canada, 2002), Vol. 7.
[43] K. Hippler, S. Sitta, P. Vogt, and H. Sabrowsky, Acta Crystallogr. Sect. C **46**, 736 (1990).
[44] J. M. Skakle, J. G. Fletcher, and A. R. West, J. Chem. Soc., Dalton Trans. 2497 (1996), doi: 10.1039/DT9960002497.
[45] D. Huang, H. Nakamura, K. Küster, A. Yaresko, D. Samal, N. B. M. Schröter, V. N. Strocov, U. Starke, and H. Takagi, Phys. Rev. Mater. **3**, 124203 (2019).
[46] A. Jain, S. P. Ong, G. Hautier, W. Chen, W. D. Richards, S. Dacek, S. Cholia, D. Gunter, D. Skinner, G. Ceder, and K. a. Persson, APL Mater. **1**, 011002 (2013).
[47] G. Kresse and J. Furthmüller, Phys. Rev. B **54**, 11169 (1996).
[48] G. Kresse and J. Furthmüller, Comput. Mater. Sci. **6**, 15 (1996).
[49] G. Kresse and D. Joubert, Phys. Rev. B **59**, 1758 (1999).

[50] J. P. Perdew, A. Ruzsinszky, G. I. Csonka, O. A. Vydrov, G. E. Scuseria, L. A. Constantin, X. Zhou, and K. Burke, Phys. Rev. Lett. **100**, 136406 (2008).
[51] S. Baroni, S. de Gironcoli, A. Dal Corso, and P. Giannozzi, Rev. Mod. Phys. **73**, 515 (2001).
[52] K. Esfarjani and H. T. Stokes, Phys. Rev. B **77**, 144112 (2008).
[53] T. Tadano, Y. Gohda, and S. Tsuneyuki, J. Phys.: Condens. Matter **26**, 225402 (2014).
[54] E. J. Candès and M. B. Wakin, IEEE Signal Process. Mag. **25**, 21 (2008).
[55] E. R. Cowley, Physica A **232**, 585 (1996).
[56] Y. Yamada and G. Shirane, J. Phys. Soc. Jpn. **26**, 396 (1969).
[57] G. Shirane and Y. Yamada, Phys. Rev. **177**, 858 (1969).
[58] R. A. Cowley, Phys. Rev. **134**, A981 (1964).
[59] S.-I. Tamura, Phys. Rev. B **27**, 858 (1983).
[60] H. Muta, K. Kurosaki, and S. Yamanaka, J. Alloys Compd. **392**, 306 (2005).
[61] S. R. Popuri, A. J. M. Scott, R. A. Downie, M. A. Hall, E. Suard, R. Decourt, M. Pollet, and J.-W. G. Bos, RSC Adv. **4**, 33720 (2014).
[62] Z. Tian, J. Garg, K. Esfarjani, T. Shiga, J. Shiomi, and G. Chen, Phys. Rev. B **85**, 184303 (2012).
[63] A. A. El-Sharkawy, A. M. A. El-Azm, M. I. Kenawy, A. S. Hillal, and H. M. Abu-Basha, Int. J. Thermophys. **4**, 261 (1983).
[64] J. He, M. Amsler, Y. Xia, S. S. Naghavi, V. I. Hegde, S. Hao, S. Goedecker, V. Ozoliņš, and C. Wolverton, Phys. Rev. Lett. **117**, 046602 (2016).
[65] B. C. Sales, B. C. Chakoumakos, R. Jin, J. R. Thompson, and D. Mandrus, Phys. Rev. B **63**, 245113 (2001).
[66] A. F. May, E. S. Toberer, A. Saramat, and G. J. Snyder, Phys. Rev. B **80**, 125205 (2009).
[67] J. Liu, Z. Dai, X. Yang, Y. Zhao, and S. Meng, J. Nucl. Mater. **511**, 11 (2018).
[68] W. Li, J. Carrete, N. A. Katcho, and N. Mingo, Comput. Phys. Commun. **185**, 1747 (2014).
[69] See Supplemental Material at http://link.aps.org/supplemental/10.1103/PhysRevB.101.184303 for phonon group velocity, phonon lifetime, Grüneisen parameter, and three-phonon scattering phase space in the four cubic antiperovskites K_3BrO, K_3AuO, Rb_3BrO, and Rr_3AuO.
[70] Y. Xia, Appl. Phys. Lett. **113**, 073901 (2018).